THE JOURNAL OF PHYSICAL CHEMISTRY C
A JOURNAL OF THE AMERICAN CHEMICAL SOCIETY

pubs.acs.org/JPCC Article

Gradually Fe-Doped Co_3O_4 Nanoparticles in 2-Propanol and Water Oxidation Catalysis with Single Laser Pulse Resolution

Swen Zerebecki, Kai Schott, Soma Salamon, Joachim Landers, Heiko Wende, Eko Budiyanto, Harun Tüysüz, Stephan Barcikowski,* and Sven Reichenberger*

Cite This: *J. Phys. Chem. C* 2022, 126, 15144−15155

Read Online

ACCESS | Metrics & More | Article Recommendations | Supporting Information

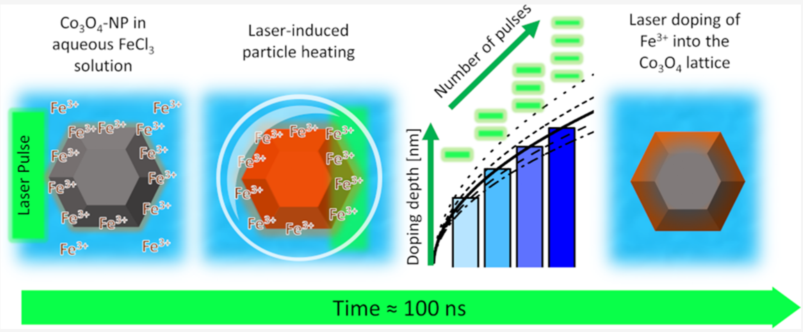

ABSTRACT: Controlling the surface composition of colloidal nanoparticles is still a challenging yet mandatory prerequisite in catalytic studies to investigate composition-activity trends, active sites, and reaction mechanisms without superposition of particle size or morphology effects. Laser post-processing of colloidal nanoparticles has been employed previously to create defects in oxide nanoparticles, while the possibility of laser-based cation doping of colloidal nanoparticles without affecting their size remains mostly unaccounted for. Consequently, at the example of doping iron into colloidal Co_3O_4 spinel nanoparticles, we developed a pulse-by-pulse laser cation doping method to provide a catalyst series with a gradually modified surface composition but maintained extrinsic properties such as phase, size, and surface area for catalytic studies. Laser pulse number-resolved doping series were prepared at a laser intensity chosen to selectively heat the Co_3O_4-NPs to roughly 1000 K and enable cation diffusion of surface-adsorbed Fe^{3+} into the Co_3O_4 lattice. The combination of bulk-sensitive X-ray fluorescence and surface-sensitive X-ray photoelectron spectroscopy was used to confirm the surface enrichment of the Fe-dopant. X-ray diffraction, magnetometry, and Mössbauer spectroscopy revealed an increasing interaction between Fe and the antiferromagnetic Co_3O_4 with arising number of applied laser pulses, in line with a herein proposed laser-induced surface doping of the colloidal Co_3O_4 nanoparticles with Fe. Using Fick's second law, the thermal diffusion-related doping depth was estimated to be roughly 2 nm after 4 laser pulses. At the example of gas-phase 2-propanol oxidation and liquid-phase oxygen evolution reaction, the activity of the laser-doped catalysts is in good agreement with previous activity observations on binary iron-cobalt oxides. The catalytic activity was found to linearly increase with the calculated doping depth in both reactions, while only catalysts processed with at least one laser pulse were catalytically stable, highlighting the presented method in providing comparable, active, and stable gradual catalyst doping series for future catalytic studies.

■ INTRODUCTION

Metal oxides are important catalysts in various industrial applications.[1] Yet, pure oxides are rarely used in a large-scale application since the introduction of a small fraction of cations or anions to host oxides typically improves their activity or selectivity. Parravano first intentionally synthesized doped oxides in 1953.[2] However, McFarland and Metiu also highlighted that most deployed oxide catalysts potentially contain low amounts of impurities or additives, which might unknowingly contribute to the performance of the catalyst,[3] rendering the identification of the active sites in heterogeneous oxide catalysts very challenging.

Co_3O_4 is a very promising oxidation catalyst for gas phase, liquid phase, and electrocatalysis, which however still only finds limited industrial use due to selectivity and stability limitations. Recent catalytic studies with pure and partially iron-substituted Co_3O_4 have shown that the catalyst performance and stability[4,5] are significantly influenced by the Fe:Co ratio,[5−7] the size,[8−11] and the shape of Co_3O_4[10,12] as well as $CoFe_2O_4$[5,13] particles. In the case of the gas-phase oxidation of

Received: March 13, 2022
Revised: August 14, 2022
Published: August 30, 2022

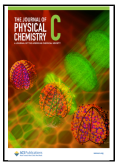

https://doi.org/10.1021/acs.jpcc.2c01753
J. Phys. Chem. C 2022, 126, 15144−15155

2-propanol over Co_3O_4, it was proposed that surface-near five-fold-coordinated octahedral Co_{5c}^{3+} acts as an active site for the oxidation to acetone.[14] Substitution of Co_3O_4 with small amounts of Fe^{3+} (<10 atom %) was shown to cause a decrease in activity in both the gas- and the liquid-phase oxidation of 2-propanol to acetone and acetic acid, respectively, since undercoordinated octahedral Co^{3+} sites are replaced by Fe^{3+}.[7] On the contrary, the electrocatalytic oxygen evolution reaction (OER) activity of iron-containing Co_3O_4 was found to slightly improve in the presence of a small atom % of iron.[5,15,16] The tetrahedral Co^{2+} cations were discussed extensively as key active sites for the formation of μ-OOH species during the OER.[5,15−18] In this context, doped Fe^{3+} replaces Co^{3+} from octahedral sites, particularly for lower iron contents which result in distortion around the cobalt centers and increased tetrahedral Co^{2+}.[5,15,18] However, higher iron contents (>13 atom %; Co:Fe ratio of 7) turned out to be increasingly detrimental, causing a gradually decreasing OER activity, which succumbs to the activity of pure Co_3O_4 when exceeding ~25 atom % iron (Co:Fe ratio of 3).[5] In this context, for higher iron contents above ~40 atom %, the replacement of tetrahedral Co^{2+} by iron ions forming the inverse spinel structure has been shown previously.[5] Additionally, at 5 atom % of Fe-doping, an activity maximum was found for the oxidation of styrene, benzyl alcohol, and cinnamyl alcohol with *tert*-butyl hydroperoxide (TBHP) as an oxidizing agent, while the activity steadily decreased over the whole iron-doping concentration when oxygen was used as an oxidizing agent.[6] The observed activity trends were discussed to highlight different activation mechanisms, such as the decomposition of the peroxide, to form reactive oxygen radicals and a spin transfer to activate the oxygen, providing new hints to identify the active site and related reaction mechanisms occurring for each oxidizing agent in future studies.[6]

In conventional synthesis methods used for the synthesis of the discussed oxide catalysts (as in the previous studies), the dopant or substituting cation (e.g., iron in Co_3O_4) is typically added during the particle synthesis to achieve bulk substitution yet potentially also affecting the particle growth (and consequently the final size) demanding careful optimization of the synthesis protocol to maintain particle size, Brunauer–Emmett–Teller (BET) surface area, and surface termination throughout the dopant series.[19] In 2D-film synthesis, on the other hand, either bulk-substituted thin-film composition libraries are gained by magnetron sputtering[20] or surface-near cation substitution is achieved by post-synthesis treatment, for example, by ion-implantation,[21] in-diffusion (from solids or gases),[22] and laser-induced doping.[23] Yet, challenges like self-purification, particularly in the case of non-thermodynamically favored dopant induction,[24] demand a limitation of the long-term heat load in order to kinetically stabilize the dopants in the lattice by fast temperature quenching.

Pulsed lasers provide an ideal tool to fulfill the previously mentioned requirements. At the example of gas-phase doping of wafers with pulsed lasers, two doping mechanisms were discussed in the past. On the one hand, in the case of p- and n-doping of Si-wafers with pulsed lasers, a thermally induced atom diffusion occurring throughout the nanosecond excitation (heating) of the laser-excited Si wafers was discussed,[25] while for laser doping of gaseous chromium precursors into SiC wafers, a laser-induced thermal stress-mediated mechanism was proposed.[26] When turning toward colloidal nanoparticles instead of wafers, as well as liquids instead of gas-phase processing, only H-doping of NiO on post-irradiation of colloidal NiO in ethanol with pulsed lasers has been reported in the past.[27] Yet, a liquid-phase laser-induced doping of cations was also discussed to occur during laser ablation,[27,28] laser fragmentation,[29] and laser melting,[30,31] where nanoparticle synthesis/growth and doping occur simultaneously. This however superimposes composition and particle properties like size or BET surface area. In turn, a laser-induced cation doping of colloidal nanoparticles by pulsed laser post-processing (PLPP) with single laser pulses and the correlation of such a surface doping with the catalytic activity still is an open field. Hereby, PLPP holds particular opportunities since it has been reported to kinetically stabilize catalysis-relevant metastable structures such as amorphous,[32,33] defective,[23] and/or single-atom catalysts[34] while maintaining the particle size and oxide phase when choosing a sufficient laser intensity regime.[35,36]

In this study, we investigated a heat-induced, diffusion-controlled pulse-by-pulse laser-doping strategy of spinel-based Co_3O_4 catalyst particles with iron cations to systematically correlate the laser-imprinted dopant surface concentration with the catalytic activity (or selectivity). Laser doping of the colloidal nanoparticles was conducted using a previously developed continuously operating flat liquid jet setup.[36] The continuous flow ensures the illumination of each colloid volume element by a single laser pulse during one passage through the setup.[36] Multiple passages allow for a gradual pulse-by-pulse processing[35,37] and hence a laser pulse-resolved doping of the colloid as well as the correlation of the doping process and the catalytic activity. The flat liquid jet geometry of the setup ensures uniform illumination conditions (laser fluence) which were found to be mandatory for maintaining the initial particle properties such as size, crystal phase, and BET area (at adequately low laser intensity).[35,37] On solving Fick's second equation considering relevant temperatures and heating times of pulsed laser heating, it will be shown that the developed laser-induced surface doping method for nanoparticles allows the control of the doping depth with the number of applied pulses. X-ray diffraction (XRD) measurements reveal an increase of the Co_3O_4 lattice parameter with the rising number of step-by-step applied laser pulses, indicating the incorporation of Fe into the Co_3O_4 lattice. HR-TEM/EDX shows the homogeneous distribution of the dopant. Utilizing XPS as a surface-sensitive method and XRF as a bulk-sensitive method, the dopant enrichment at the surface was confirmed. The diffusion of surface Fe into Co_3O_4 was tracked with magnetometry and Mössbauer spectroscopy measurements while using isotope-pure ^{57}Fe as the dopant. The doped catalysts were tested in the 2-propanol oxidation and the electrochemical OER, revealing an increase in activity after the laser treatment in correlation with the doping depth.

■ EXPERIMENTAL DETAILS

300 mg of Co_3O_4 powder (<50 nm, Merck 637025) was ground, dispersed in 1 L of Milli-Q water containing 0.5 and 2 mmol/L $FeCl_3$, and finally sonicated for 60 min using an ultrasonication bath. The pH value of the dispersion was kept at around 2.7–3.3 to ensure that Fe^{3+} remains dissolved as Fe^{3+}, $Fe(OH)^{2+}$, and $Fe(OH)_2{}^+$ while avoiding potential precipitation as $Fe(OH)_3$ which would occur above pH 5.[38]

Pulsed Laser Post-processing. To initiate Fe-doping of the Co_3O_4 particles, the as-prepared dispersion was irradiated by a 532 nm pulsed laser (IS400-1-L, SHG, Edgewave) with a pulse duration of ~7 ns and a repetition rate of 5 kHz. The PLPP was performed in a continuous-flow flat jet setup to enable uniform irradiation under one pulse per volume element condition.[36] Hereby, the beam was modified by truncation to gain a more rectangular beam profile with a spot size of 0.3709 mm^2 (see Figure S1), which resulted in a laser intensity of ~0.6×10^{11} W m^{-2}. The width of the truncated beam matched the distance of the Teflon knives that were installed to cut out the laser-irradiated volume fraction of the flat liquid jet which contained the nanoparticles that were to be laser-processed (−doped). The non-irradiated part of the liquid at the outside of the Teflon-knife setup was recycled back into the educt-containing vessel for further processing as described previously.[36] After the treatment, laser-doped nanoparticles and the liquid phase were separated by centrifugation at 15,000 rpm for 60 min. The nanoparticle pellet that was gained by centrifugation was dispersed in Milli-Q water 3 times, whereby it was repeatedly centrifuged and redispersed with fresh Milli-Q water to remove any excess Fe- and Cl-ions to be subsequently freeze-dried.

To obtain Mössbauer spectra with sufficient resolution even at very low overall Fe content, a pulse-by-pulse-resolved laser-doping series was prepared with a 0.5 mmol/L $FeCl_3$ precursor solution only containing iron as the ^{57}Fe isotope (enriched to >95%, Chemotrade GmbH). This strongly increases the fraction of resonant nuclear absorption while not altering the chemical properties of the resulting particles. The $^{57}FeCl_3$ solution was prepared by dissolving metallic ^{57}Fe in 30% HCl and 30% H_2O_2. The dissolved $^{57}Fe^{3+}$ was then precipitated with NaOH as $^{57}Fe(OH)_3$ and washed with Milli-Q water 3 times by centrifugation. $^{57}Fe(OH)_3$ was dissolved in a pH 3 HCl solution and utilized for Fe-doping of Co_3O_4 particles in the same manner as described for the previously specified $FeCl_3$ solution.

Material Characterization. High-resolution transmission electron microscopy (HRTEM) and energy-dispersive X-ray spectroscopy (EDX) were performed with a JEOL JEM 2200FS equipped with a chemiSTEM EDX detector system.

X-ray photoelectron spectroscopy (XPS) measurements were carried out with a PHI 5000 Versaprobe II utilizing a monochromatic aluminum anode with a $K\alpha$ line at 1486.6 eV, a spot size of 100 μm, a hemispherical analyzer (with an angle of 45° between the surface of the sample and the analyzer), and dual beam charge neutralization. All XPS spectra were referenced to the C 1s signal of hydrocarbons (284.8 eV) found in every corresponding sample. Baseline correction (Shirley) and fitting of the corrected XPS signals were conducted with Casa XPS.

XRD measurements were conducted on a D8 ADVANCE (Bruker) powder diffractometer with Cu $K\alpha$ radiation (λ = 0.15418 nm, 40 kV, and 40 Ma). The cell parameter and the size of the coherent diffraction domain were determined with MAUD software which is based on the Rietveld method combined with Fourier analysis, well adapted for broadened diffraction peaks. LaB_6 was used as a standard to quantify the instrumental broadening contribution.

Mössbauer spectra were recorded in transmission geometry on powder samples using a $^{57}Co(Rh)$ radiation source mounted on a constant acceleration driving unit. Low temperatures and high magnetic fields were achieved using a liquid helium bath cryostat, containing a superconducting solenoid in split-pair geometry, thereby allowing measurements at 4.3 K under a magnetic field of 5 T applied parallel to the γ-ray propagation direction. All spectra were evaluated using the "Pi"-program package.[39]

Diffuse reflectance infrared Fourier transform spectroscopy (DRIFTS) measurements were performed with a Nicolet iS50R FT-IR equipped with a FTIR-reaction chamber, see Figure S11. A background spectrum was recorded before each measurement with 10 mg KBr, which was preheated at 400 °C for 30 min under a constant synthetic dry air flow and then measured at 100 °C. For in situ 2-propanol oxidation, ~10 mg of catalyst was preheated in the sample holder at 300 °C for 30 min under steady synthetic dry air flow (2 mL/min). After the heat treatment, the temperature was reduced from 300 to 30 °C, and the catalyst was then exposed to a saturated 2-propanol/synthetic air mixture for 5 min (2 mL/min flow). Subsequent purging with synthetic dry air for 10 min assures the removal of unbound as well as reversible adsorbed 2-propanol from the sample surface and the reaction chamber. To realize steady batch process-like reaction conditions, synthetic air flow was turned off. The oxidation of the 2-propanol adsorbed on the catalyst surface was initiated by ramping the temperature from 30 to 230 °C (2 °C/min) while every minute a DRIFT spectrum was acquired in a range between 500 and 4000 cm^{-1} with OMNIC (FTIR software).

Electrochemical OER measurements were performed with a BioLogic VSP-300 Potentiostat coupled with a rotating disc electrode (Model: AFMSRCE, PINE Research Instrumentation) using a three-electrode system. Pt wire was used as the counter electrode and a hydrogen reference electrode (Hydro-Flex, Gaskatel) as the reference electrode. The measurement was done in alkaline conditions using 1 M KOH as the electrolyte. The working electrodes were prepared by depositing electrocatalyst ink onto glassy carbon (GC) electrodes (5 mm diameter, 0.196 cm^2 geometric surface area, PINE Research Instrumentation). Before the catalyst deposition, GC electrodes were polished with alumina micropolish suspension (1 and 0.05 μm, Buehler). To prepare ink, 4.8 mg of electrocatalyst powder was dispersed in 0.75 mL of Milli-Q water (18.2 MΩ.cm) and 0.25 mL of isopropanol. 50 μL of Nafion 117 (Sigma Aldrich) was then added to the dispersion as the binding agent followed by sonication for 30 min to get a homogeneous ink. Finally, 5.25 μL of the ink was drop-cast onto a clean GC electrode surface and dried under lamp radiation and Ar flow (the calculated catalyst loading was equal to 0.12 mg/cm^2). The linear scan voltammetry (LSV) curve was measured at the scan rate of 10 mV/s within the potential bias of 0.7−1.7 V vs RHE and working electrode rotation speed of 2000 rpm. Cyclic voltammogram was recorded at the scan rate of 50 mV/s within the potential bias of 0.7−1.6 V vs RHE. The IR drop was compensated at 85% for all measurements.

■ RESULTS AND DISCUSSION

Characterization of Laser-Doped Materials. HR-TEM/EDX images of the dry Co_3O_4 particles after the dispersion in 2 mmol/L $FeCl_3$ and 3 times washing with Milli-Q water are displayed in Figure 2a−d. The HR-TEM image shows that small clusters have formed on top of the Co_3O_4 crystals (see Figure 2a,b). Samples impregnated with 0.5 mmol/L dopant solutions did not indicate the formation of these clusters (compare Figure S2). EDX investigation of the high dopant concentration impregnation (2 mmol/L $FeCl_3$) shows red-colored particle edges in Figure 2c. A quantification suggests the presence of ~21 atom % of the adsorbed iron precursor on the surface after the impregnation and washing steps. Consequently, the clusters observed in HR-TEM after Fe^{3+} impregnation likely resemble FeO(OH) clusters that formed from the adsorbed ions[40,41] when the samples were dried during TEM grid preparation. The former is confirmed in the EDX-line scan (Figure 2d), where indications of Fe can only be found outside of Co_3O_4. Although none of the clusters were observed in the case of samples impregnated by the low dopant concentration of 0.5 mmol/L, still 5−6 atom % of Fe was found after impregnation and washing (compare Figure S2c).

Pulse-by-pulse laser doping of the colloidal Co_3O_4 sample with Fe^{3+} cations was conducted in several subsequent passages of the colloidal Co_3O_4 dispersion through a self-developed flat liquid jet setup. This setup is depicted in Figure 1 and mainly consists of a flat jet nozzle that produces a ~130 μm thin planar liquid layer.[36] Pulsed laser irradiation through this planar layer results in a uniform irradiation of the colloidal particles due to their low thickness while minimizing the laser diffraction and distortion at the liquid layer surface as described elsewhere.[36] A detailed discussion of the laser intensity distribution and the comparison to a simple round jet was published previously.[36] The flat jet setup has successfully been employed for pulsed laser defect engineering of Co_3O_4[35] and $CoFe_2O_4$[37] in water under single laser pulse conditions. In both studies, it was shown that the crystal defect density was gradually increased with each laser pulse, while the BET surface area, nanoparticle morphology, and spinel phase were maintained under the chosen laser processing conditions. The setup enables us to apply an individual laser pulse with uniform laser intensity to each volume element (containing the iron-impregnated colloidal Co_3O_4 nanoparticles) that passes through the illuminated cross-section.[36] Gradual laser pulse-resolved Co_3O_4-doping series were prepared with Fe^{3+} whereby a pulse-by-pulse laser treatment was conducted at the example of two precursor concentrations (0.5 mmol/L $^{57}FeCl_3$ and 2 mmol/L $FeCl_3$, respectively). For each precursor concentration the colloid successively passed through the setup in 1−4 passages and was irradiated with a single laser pulse per passage. For the high precursor concentration of 2 mmol/L, HR-TEM and EDX investigations after pulse-by-pulse laser treatment with 1 and 4 laser pulses (passages) are shown in Figure 2e—l, respectively. As can be seen, after pulse-by-pulse processing of the colloidal Co_3O_4 nanoparticles with a single or multiple subsequent laser pulses, the FeO(OH) clusters disappeared. Yet, EDX mapping of laser-doped samples (Figure 2g,k) indicates that iron is still located in the surface-near regions of the Co_3O_4 sample. However, the Fe signals appear to have weakened or spatially broadened upon laser treatment, particularly visible within the EDX-line scans (Figure 2h,l), which renders the determination of the Fe-dopant location from EDX investigation rather difficult. Additionally, after laser treatment, a disordered surface layer seems to be recognizable in the HR-TEM pictures in Figures 2f,j and S2f,j, which was also previously observed for laser-treated $CoFe_2O_4$ and assigned to the presence of surface hydroxides.[37]

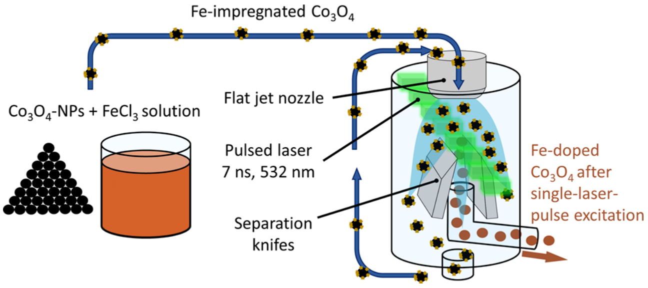

Figure 1. Scheme on the performed laser doping of Co_3O_4 with Fe^{3+} cations under single pulse per particle condition.

To discriminate the presence of Fe in the surface and within the overall sample, both XPS and XRF analyses were conducted, respectively. Hereby, XPS can be considered a surface-sensitive method. In the case of an epitaxially grown Co_3O_4 film, a comparable excitation angle of 45° used here, and the given X-ray source intensity, Vaz et al. determined the information depth to be 1−2 nm[42] representing the well-known high surface sensitivity of XPS. Yet, to avoid later misconceptions, it stands to be noted that XPS does not represent the composition of the first surface layer alone but resembles an average composition over several surface layers. Contrarily, the information depth of XRF is in the range of more than 1 μm, which significantly exceeds the particle diameter of <50 nm, rendering XRF sensitive to the overall particle composition.[43]

The analysis results for both gradual laser pulse-resolved Co_3O_4-doping series impregnated at iron precursor concentrations of 0.5 and 2 mmol/L, respectively, are summarized in Figure 3a. Considering all investigated samples, the atom % of iron determined from the Fe 3p and Co 3p XPS signal (see Figure S4) was found to be 2−6 times higher than the iron content found with XRF, indicating a high concentration of iron in the first surface layers of the laser-processed Co_3O_4 particles. Furthermore, when Co_3O_4 was impregnated with 2 mmol/L $FeCl_3$, a particularly high surface iron content, indicated by the surface to bulk iron ratio in the inset of Figure 3a, is observed by XPS before the first laser pulse is being applied. This observation coincides well with the iron clusters observed in TEM (Figure 2b). In turn, the sample impregnated with 0.5 mmol/L $FeCl_3$ shows a 5 times lower initial iron content on the surface (Figure 3a) and no clusters on the surface (compare Figure S2b). After applying the first laser pulse, the Fe content significantly decreases when a dopant concentration of 2 mmol/L $FeCl_3$ was used, while for 0.5 mmol/L $FeCl_3$, the Fe content slightly increases. Hence, for the sample impregnated with 2 mmol/L $FeCl_3$, respectively, the presence of iron clusters, the high initial iron surface content, and the decrease of the surface iron content after the first laser pulse all indicate that the laser-induced doping process is superimposed by partial laser-induced dissolution/desorption of the iron precursor from the Co_3O_4 surface after the first laser pulse for the high $FeCl_3$ educt concentration. In turn, for the 0.5 mmol/L sample, the absence of iron clusters, comparably lower initial iron surface content, and the fairly constant amount of iron on the surface after the first laser pulse point toward the absence of such partial iron dissolution at these low iron concentrations. To further elucidate the interpretation of a potential laser-induced dissolution/desorption at a higher concentration of $FeCl_3$, a concentration series was prepared and investigated by XRF (shown in Figure S3) before and after employing the first laser pulse. In the case of $FeCl_3$-concentrations between 0.01 and 0.5 mmol/L (and subsequent 3× washing in Milli-Q water), the Fe content on Co_3O_4 remained relatively constant at 2−3 wt % independent

https://doi.org/10.1021/acs.jpcc.2c01753
J. Phys. Chem. C 2022, 126, 15144−15155

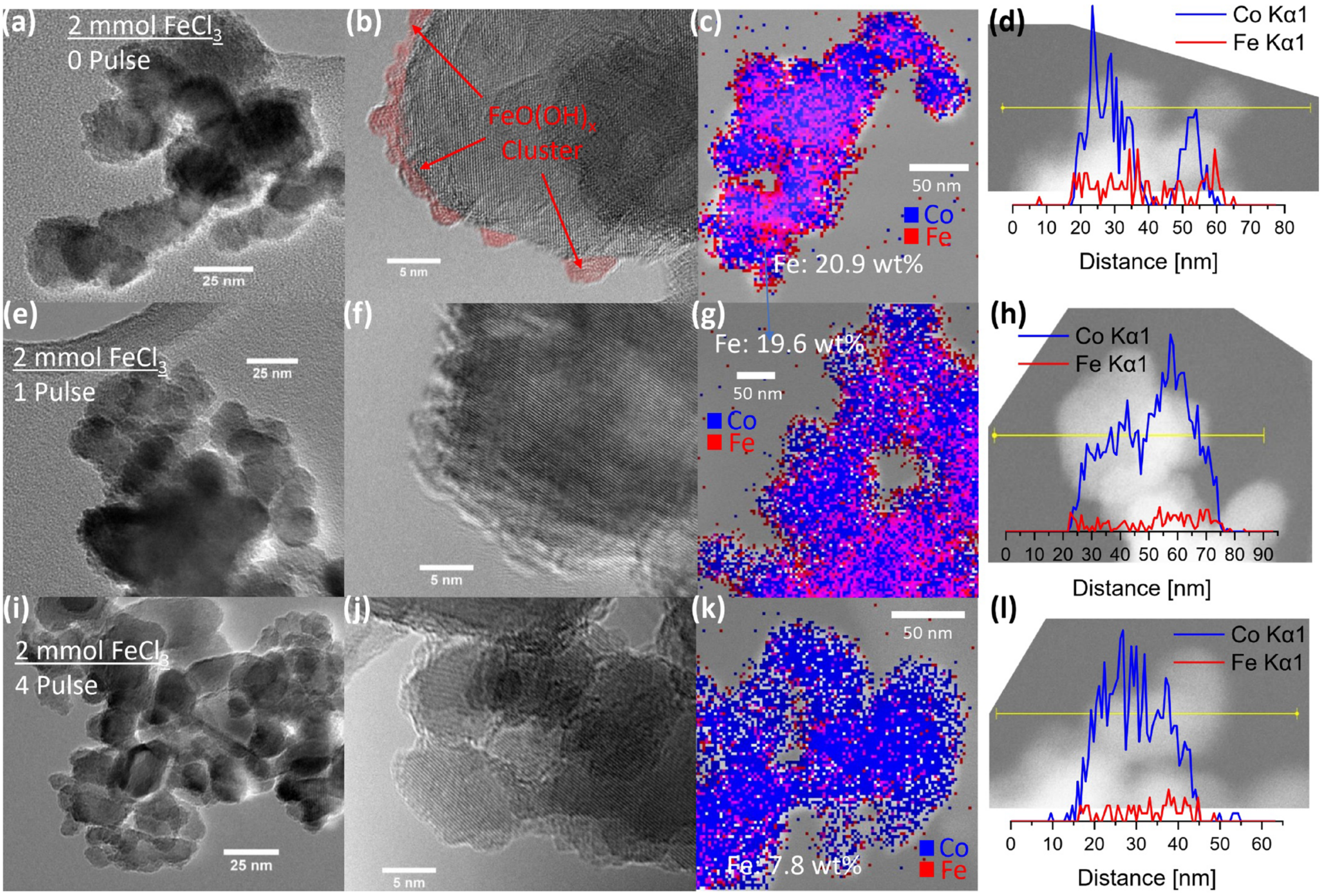

Figure 2. HR-TEM/EDX images of Co_3O_4 after dispersion and separation from a 2 mmol FeCl3 solution. (a–d) Without laser treatment. The FeO(OH) clusters from the impregnation of Co_3O_4 with the Fe^{3+} precursor before laser treatment are colored red in (b). After laser treatment: (e–h) with 1 pulse and (i–l) with 4 applied pulses.

of whether a single laser pulse was employed or not, while for 1 and 2 mmol/L $FeCl_3$, the Fe content increases up to 20 wt % upon impregnation and decreases by a factor of ~2 upon laser treatment of the 2 mmol/L impregnated samples (see Figure S3). This indicates that a partial laser-induced dissolution/desorption of Fe cations on laser processing is neglectable for lower iron concentrations but becomes more pronounced above 1 mmol/L of the dopant precursor solution. It is likely that for higher concentrations either the monolayer adsorption of iron on the colloidal Co_3O_4 nanoparticles was exceeded or the electrochemical double layer around the respective colloidal nanoparticles was oversaturated with iron cations. For the high 2 mM, $FeCl_3$ dopant concentrations and the first laser pulse, the excess iron is removed (dissolved) in addition to the diffusion of iron into the laser-heated Co_3O_4 lattice. The absence of iron clusters after the first laser pulse, which would be expected due to adsorption of the partial iron fraction, dissolved by the laser pulse points toward an altered surface that is mediated by laser-induced iron doping, rendering reabsorption less favorable. As indicated by XPS and XRF, the following laser pulses only slightly change the overall Fe content. Assuming laser-induced doping, the former suggests that the Fe-ions are distributed within the surface near the Co_3O_4 lattice. The constant surface composition observed from XPS spectroscopy further leads to the conclusion that the maximum diffusion depth that can be reached by up to 4 laser pulses should be below the information depth of the XPS (~2 nm).

The XRD spectra of pulse series at low (0.5 mmol/L) and high (2 mmol/L) dopant concentrations show that no additional phases besides the initial Co_3O_4 are observed in Figures S5 and S6. Furthermore, the FeO(OH) clusters seen in the TEM (Figure 2b) were not observed in XRD, which indicates that they were either too small (signals too broad) to be detected or were present in an amorphous form. Yet, interestingly, a slight but significant shift of the Co_3O_4 spinel signals toward smaller 2θ angles can be observed in Figures S5b and S6b with an increasing number of employed laser pulses. This indicates an expansion of the unit cell which was further investigated by performing a Rietveld refinement of the XRD patterns.

The lattice parameter of the samples within the laser pulse series of both, high and low dopant concentrations was determined by Rietveld refinement and is shown in Figure 3b. Particularly for the high dopant concentration, a gradual increase in the lattice parameter is found with an increasing number of single laser pulses considering the error bars determined from the fitting quality of the Rietveld refinement. In the case of a low dopant concentration, only pulse-by-pulse laser doping with more than two laser pulses indicates a slight increase. Considering that the lattice parameter of $CoFe_2O_4$ is ca. 8.38 Å, an increase of the average lattice parameter from 8.086 to 8.091 Å would indicate that when averaging over the

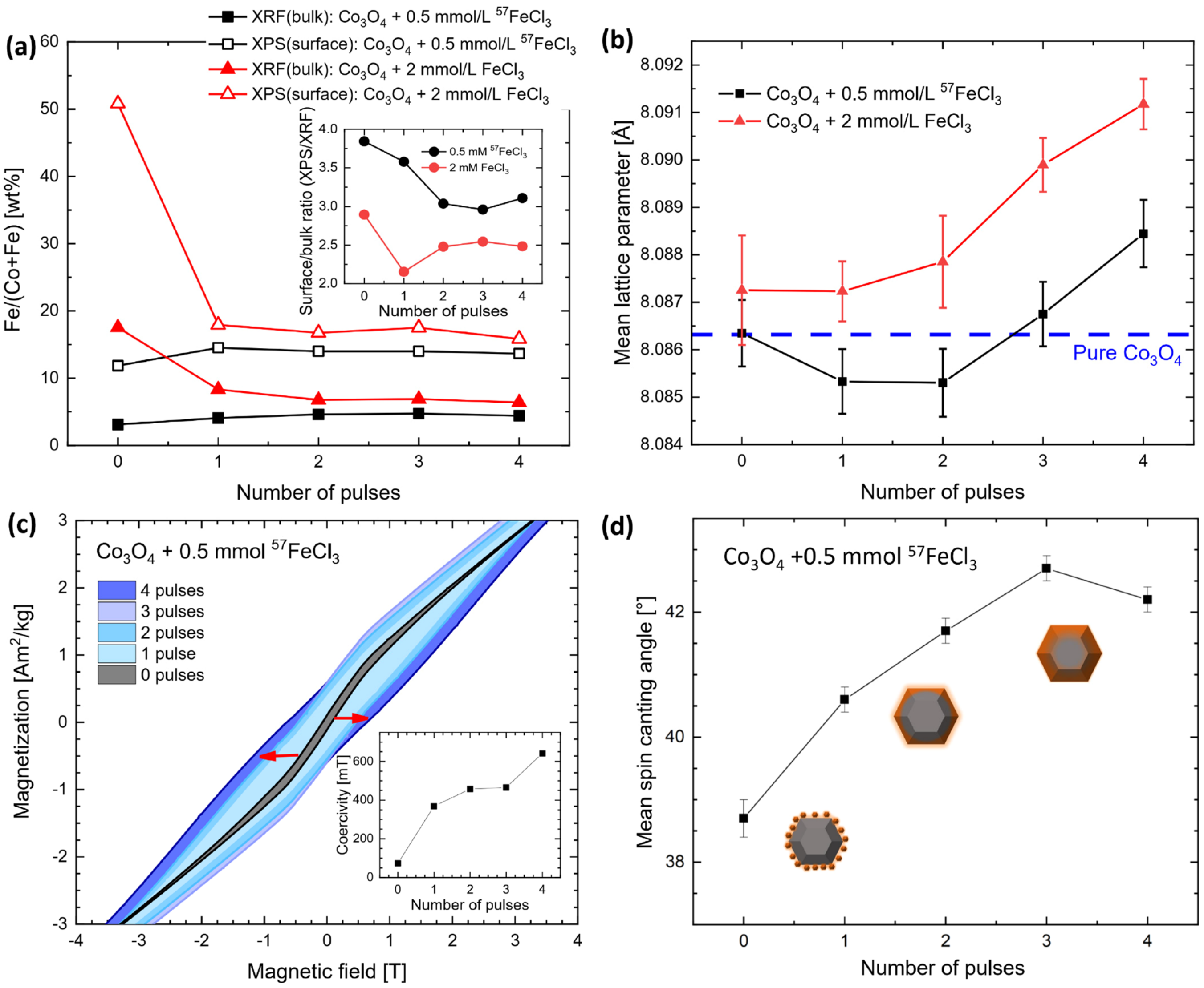

Figure 3. (a) Iron content determined via XRF (bulk) and XPS (surface) from two sample series with an increasing number of applied laser pulses, prepared in a 2 mmol/L $FeCl_3$ and a 0.5 mmol/L $^{57}FeCl_3$ solution. (b) The lattice parameter was determined from XRD Rietveld refinement for the two sample series. (c) Magnetization hysteresis from magnetometry measurements at 4.3 K of the ^{57}Fe-enriched sample series; the inset shows the coercivity vs number of laser pulses (see Figure S7 for the full-field range). (d) Mean spin canting angle determined from Mössbauer spectroscopy at 4.3 K and 5 T.

whole particle volume, ~1 to 2 atom % of Fe was doped into the Co_3O_4 lattice. Note that this iron content resembles the iron that (i) was potentially incorporated into the lattice and (ii) represents an average over the whole nanoparticle volume. In turn, the bulk-sensitive XRF results represent the sum of all iron (adsorbed on the Co_3O_4 surface and potentially laser-doped) and hence provide significantly higher iron contents. Finally, when comparing the size of the crystalline domains of pulse-by-pulse laser-doped samples (see Table S1), the domain size appears to remain unchanged at 38−39 nm for all samples. This confirms that no undesirable size change due to laser fragmentation or melting occurred during pulse-by-pulse laser processing of the iron precursor-impregnated colloidal Co_3O_4, respectively.

To further investigate potential laser-induced iron incorporation into the Co_3O_4 spinel structure, the samples that were laser-processed in the 0.5 mmol/L $^{57}FeCl_3$ precursor solution were investigated by magnetometry (Figures 3c, S7, and S8) and Mössbauer spectroscopy (see Figures 3d, S9, and S10). Magnetization curves recorded at 4.3 K display a gradually (linearly) increasing coercivity (compare Figure 3, inset) and remanence with the number of employed laser pulses. Note that the increase of the magnetization hysteresis would also be expected in the case of an increase in ^{57}Fe content, yet the XRF and XPS results in Figure 3 show a constant Fe content (within the range of ±1 wt %) with an increasing number of pulse-by-pulse laser doping. Hence, the results in Figure 3 indicate the presence of increasingly more uncompensated magnetic moments within the antiferromagnetic Co_3O_4, which points toward the incorporation of iron into the Co_3O_4 spinel after single and repeated laser-induced excitation.

To further probe the magnetic environment around Fe^{3+}, Mössbauer spectra were recorded at 4.3 K and an applied magnetic field of 5 T and display an asymmetric sextet structure (see Figure S9) mainly independent of laser treatment, which exhibits an average isomer shift of ca. 0.43 mm s^{-1} relative to that of α-Fe at room temperature. This observation can be attributed to Fe^{3+} states originating from

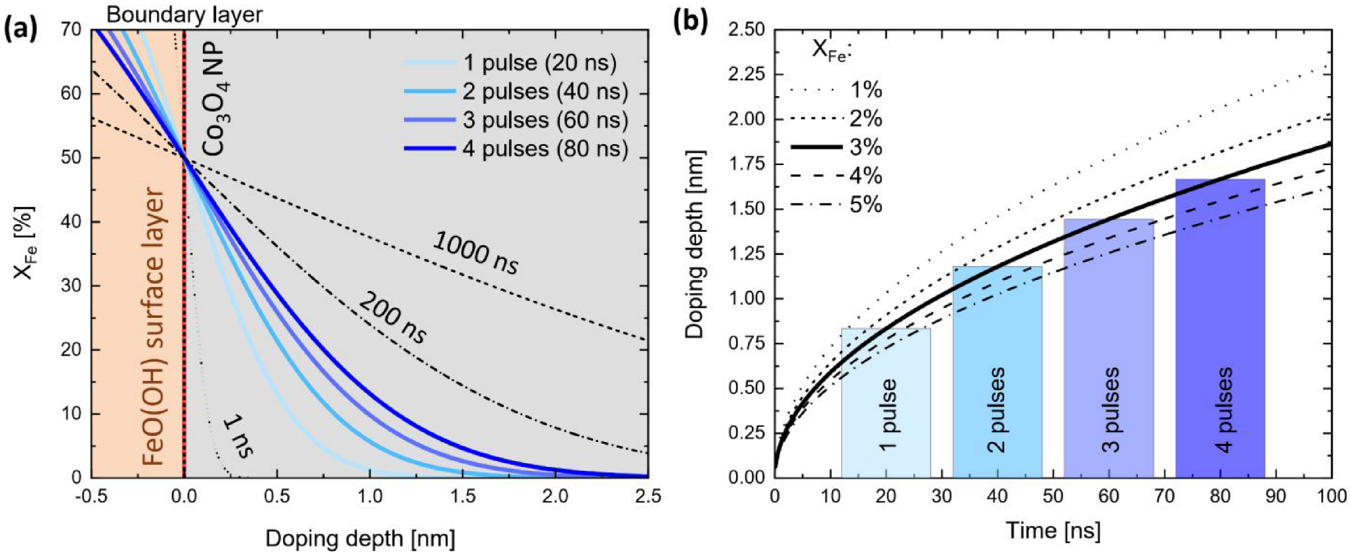

Figure 4. (a) Calculated Fe-concentration profiles for the FeO(OH)/Co_3O_4 interface after nanosecond pulsed laser heating. (b) Calculated time-dependent doping depth for different threshold concentrations between 1 and 5%.

the atom clusters at the particle surface that presumably represent the intermediary Fe^{3+}-reservoir. Regarding laser pulse-driven Fe-transport, one can observe a moderate increase in the relative line intensity ratio A_{23} being particularly prominent for the first laser pulse, which is indicative of the average spin alignment relative to the external magnetic field (Figure S10). A minor increase after the first laser pulse is also visible regarding the average hyperfine magnetic field. The average canting angles shown in Figure 3d are extracted from A_{23} (Figure S10b).[44] The observed increase in spin frustration upon laser treatment supports the previous interpretation drawn from XRD that a fraction of Fe atoms were continuously incorporated into the antiferromagnetic Co_3O_4 material, where they do not display magnetic alignment, being consistent with results from magnetometry.

The previous XRD and Mössbauer results increasingly indicate that a successful gradual laser-induced pulse-by-pulse doping of Co_3O_4 with the initially adsorbed Fe^{3+} precursor cations occurred. Yet, the question remains if the diffusion of Fe-ions into the Co_3O_4 lattice heated by an individual laser pulse with a pulse duration of ~7 ns is possible, considering that the time frame where the particle temperature is sufficiently high to promote cation exchange and diffusion is limited to 10−20 ns.[45] Note that the diffusion coefficient, however, rises exponentially with the temperature.[46]

Modeling of the Laser-Induced Cation Diffusion. To estimate the possible diffusion depth initiated by a single laser pulse, we used the common error function solution for Fick's second law to gain the time-dependent diffusion under consideration of the concentration gradient.[47] Hereby, the employed error function $\mathrm{erf}(y) = \frac{2}{\sqrt{\pi}} \int_0^y e^{-z^2} dz$ also considers interdiffusion:[48]

$$c(x,\, t) = \frac{c_s + c_b}{2} - \frac{c_s + c_b}{2} \mathrm{erf}\left(\frac{x}{2\sqrt{Dt}}\right) \quad (1)$$

We estimate the mole fraction of Fe on the surface to be $c_s = 1$ and in the bulk, $c_b = 0$, therefore writing eq 1 as

$$c(x,\, t) = \frac{1 - \mathrm{erf}\left(\frac{x}{2\sqrt{Dt}}\right)}{2} \quad (2)$$

Within the calculation, we approximated the chemical diffusion coefficient of cation vacancies in Co_3O_4 ($D \approx 5 \cdot 10^{-8}$ cm^2 s^{-1}) determined at 1000 K by Grzesik et al.[49] Co_3O_4 is a p-type semiconductor, and the used 532 nm 7 ns laser pulses excite a charge transfer (CT) from $p(O^{2-}) \rightarrow t_2(Co^{2+})$.[50,51] These CT excitations are expected to quickly decay within 3 ps due to a strong electron−phonon coupling,[52] causing the particle temperature to rapidly increase. The reached temperature is comparable to previously combined Mie- and two-temperature model calculations of the laser heating of Co_3O_4 with comparable laser intensity.[35] However, note that a deviation of ±200 K from the estimated temperature would increase or decrease the chemical diffusion coefficient by an order of magnitude.[49] Following the study of Furlani et al. that provide insights on the time frame, the particles remain hot at different nanosecond pulse durations, it is reasonable to expect that the particles remain hot for a duration of ~3 times the pulse duration[53] (in our case ~20 ns) per employed laser pulse. Based on this time frame, Figure 4 shows an estimation of the Fe-concentration profiles initiated by laser-induced thermal cation diffusion.

It appears unlikely that Fe^{3+} only occupies interstitial sites or cation vacancies. Hence, in this model, the iron concentration at the FeO(OH)/Co_3O_4 interface ($x = 0$) was set to 50% (see Figure 4a) which assumes that doping was mainly driven by an interdiffusion of iron into the Co_3O_4 lattice thereby replacing cobalt ions that subsequently diffuse out of Co_3O_4 and desorb into the surrounding solution. The calculated doping depth shows a logarithmic increase with the diffusion time (and hence the number of laser pulses) as can be seen in Figure 4b for different concentration thresholds. Therefore, the first applied laser pulse introduces the biggest doping depth (at 3 atom % Fe) of up to 0.8 nm which equals about two surficial Co_3O_4 spinel layers. If a deviation of the estimated temperature by ±200 K is assumed for the full duration, the doping depth initiated by the first laser pulse (at 3 atom % Fe) could vary between 0.3 and 2.7 nm for the lower or higher temperatures,

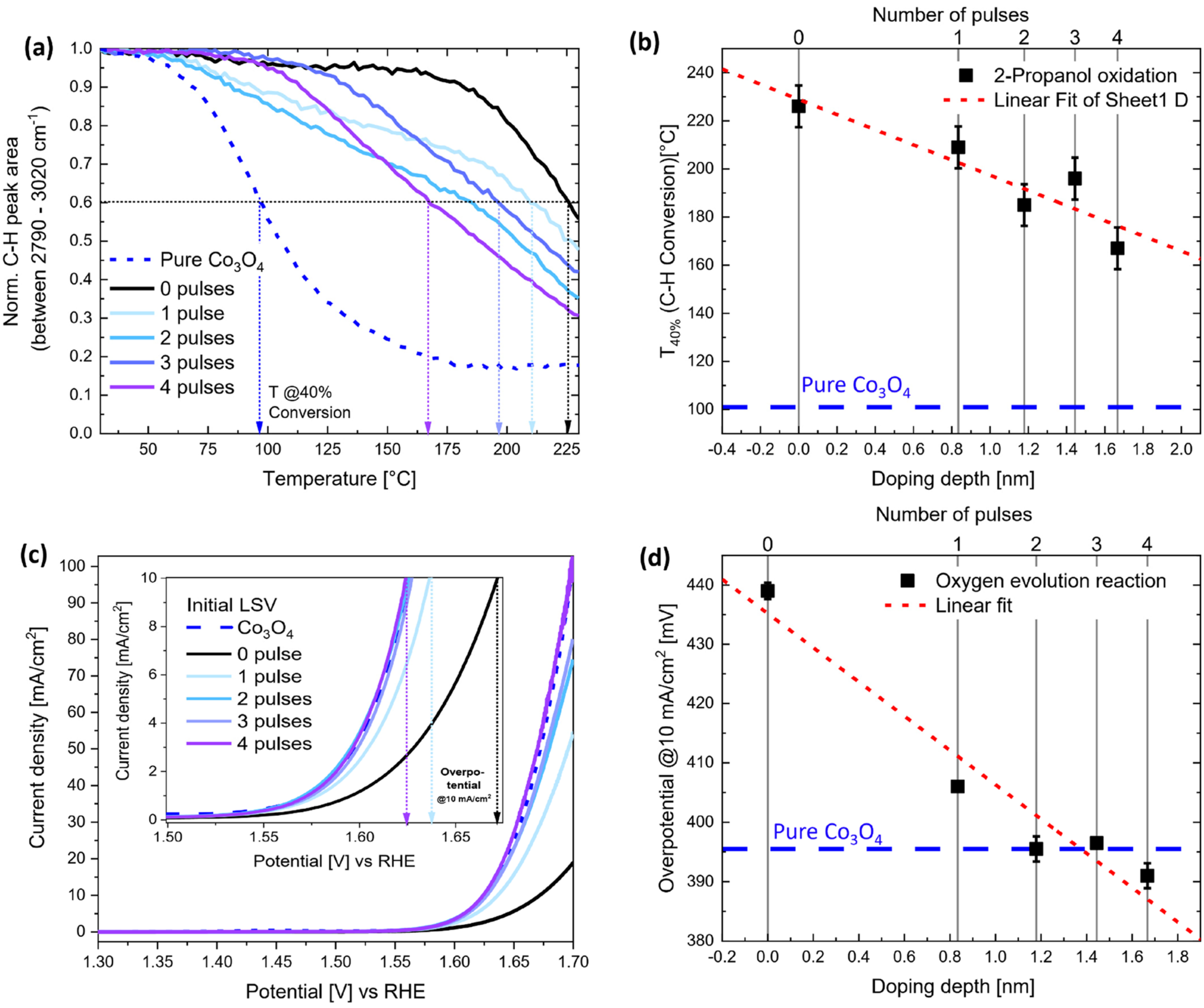

Figure 5. Comparison of the catalytic activity of nanoparticulate Co_3O_4 gradually laser-doped pulse-by-pulse in 2 mmol/L iron precursor concentration: (a) Temperature-dependent conversion of 2-propanol in gas-phase oxidation indicated by the normalized C−H peak area (to peak area at 30 °C representing the situation of negligible conversion) investigated by DRIFTS and (b) characteristic activity parameter for the selective 2-propanol oxidation ($T_{40\%}$); OER in the liquid phase, (c) linear sweep voltammograms, and (d) related overpotential at 10 mA/cm^2 for a gradually increasing number of laser pulses proportional to the Fe cation doping depth.

respectively. Even though this estimation does not intend to provide exact predictions (considering the number of assumptions that had to be used), it yet shows that a laser-induced thermal diffusion of iron cations into Co_3O_4 does occur on reasonable orders of magnitude to expect gradual pulse-by-pulse surface doping of the processed spinel catalysts. This further supports the interpretation of an increasing doping depth (and dopant concentration shown in XRD) with the rising number of laser pulses previously inferred from XRD (Figure 3b) and Mössbauer spectroscopy studies (an increase of the average spin canting angles as visible in Figure 3d). Furthermore, the coercivity shown in the inset of Figure 3c roughly follows a logarithmic increase as well, which is in very good agreement with the estimated thermally induced diffusion-depth profiles in Figure 4b. Finally, since the bulk composition was mainly unchanged after the first laser pulse (XRF in Figure 3a), the highest doping depth expected by laser-induced thermal iron diffusion (~1,8 nm; Figure 4b) is well in line with the XPS information depth (~2 nm) while also showing a constant XPS surface composition. This suggests that the first laser pulse infused the surface-near Co_3O_4 layers with the adsorbed iron, while the subsequent laser pulses further distributed the iron ions into the sub-surface.

Catalytic Investigation. To evaluate the effect of the iron doping concerning the catalytic activity of the pulse-by-pulse laser-doped Co_3O_4 catalysts (in 2 mmol/L $FeCl_3$), their respective activity was investigated in two different reactions, namely, the gas-phase 2-propanol oxidation and the liquid-phase electrochemical OER. The 2-propanol oxidation was performed via an in situ DRIFTS measurement at 2 °C intervals between 30 and 230 °C (details are described in Supporting Information, Figure S11−S13). As shown in Figure S12, several of the recorded DRIFTS peaks could be assigned to the different intermediate and product species of the 2-propanol oxidation. The development of the respective peak area of these species with increasing temperature is shown in Figure S13. Figure 5a shows the calculated normalized C−H peak areas that were gained from the DRIFTS study performed with the catalysts doped with different numbers of laser pulses. Normalization of the C−H peak area was performed concerning the peak area at 30 °C where no conversion can be observed. From the activity profiles in Figure 5a, the $T_{40\%}$ value was chosen as an activity-related coefficient representing the temperature where the initial C−H peak area (C−H bonds in 2-propanol or of intermediates to CO_2) was reduced by 40% (over a temperature ramp of 2 K min^{-1}). Subsequently, the respective activity parameter ($T_{40\%}$) of each investigated laser-doped sample was plotted against the previously estimated doping depth (see Figure 5b) for a gradually increasing number of pulse-by-pulse laser-doping steps (from solving Fick's second law and consideration of a projected effective laser-induced temperature at given laser intensity and heating time at a given pulse duration, compare Figure 4b). Furthermore, the activity of the same catalyst series was also determined for the liquid-phase OER from linear sweep voltammograms shown in Figure 5c and summarized in Figure 5d by plotting the overpotential at 10 mA/cm^2 against the estimated, increasing doping depth.

Comparing both reaction profiles (gas-phase isopropanol oxidation and liquid-phase OER) in Figure 5b,d, respectively, the doped catalysts show a linear improvement of the catalytic activity with rising calculated dopant depth (proportional to the gradual increase of the number of applied laser pulses indicated as the upper x-axis in Figure 5b,d) in both reactions. In the case of the 2-propanol oxidations, all Fe-doped catalysts performed worse than the pure Co_3O_4 which is in agreement with the previous literature since particularly for non-laser treated iron-impregnated Co_3O_4, the active site (five-fold-coordinated Co^{3+}_{5c})[14] is being displaced and blocked by less active Fe^{3+}.[6,7] For pure Co_3O_4, the temperature of roughly 100 °C at 40% conversion matches the literature; however, the decrease in activity upon laser-induced surface Fe doping seems more pronounced.[7] Since especially the first atomic layers strongly affect the catalytic activity, the observed gradual increase in catalytic activity with ongoing pulse-by-pulse doping (increasing number of laser pulses and expected doping depth) and the related laser-induced interdiffusion of iron into the Co_3O_4 lattice potentially decrease the density of detrimental Fe^{3+} surface clusters on the catalyst surface. Respective conclusions are in strong agreement with those drawn from the increasing mean spin canting angle observed in Mössbauer spectroscopy (Figure 3d). Yet, it stands to be noted that Mössbauer spectroscopy was performed with samples doped with low-concentrated (0.5 mmol/L) ^{57}Fe cations to be more sensitive to magnetic Fe−Co interactions, while the catalytic activity was analyzed for samples doped at a higher cation concentration of 2 mmol/L to ensure a sufficient sensitivity of this analysis to the presence of iron.

In any case, the same trend is observed for the OER activity (Figure 5d), where the sample doped with 4 individual laser pulses and containing ~17 atom % of Fe in the first 1−2 nm (XPS information depth[42]) even shows an exceeding activity compared to the initial Co_3O_4 that was completely untreated. These results are in line with the most recent investigation of Fe-doped Co_3O_4 from Tüysüz and co-workers, who observed an optimum activity at about 3 atom % (Co/Fe ratio of 32)[5] of bulk iron-substituted Co_3O_4 spinel synthesized via the hard-templating method, while the sample containing ~13 atom % Fe (Co/Fe ratio of 7)[5] was still slightly more active than pure Co_3O_4 in line with our results. However, their Co/Fe 7 catalyst performed better with a reported overpotential of 378 mV at 10 mA/cm^2.[5] They explain this increase in activity with an increasing ratio of Co^{2+} on the tetrahedral sites compared to Co^{3+} on the octahedral sites, where the tetrahedral ones were proposed as an active site for the formation of μ-OOH moieties in the intermediate state of OER.[54] The tetrahedral to octahedral occupation ratio increase might occur due to the displacement of Co on the octahedral sites by Fe, which at a low amount could also enhance the conductivity of the cobalt-iron oxyhydroxide intermediate active state during the applied potential bias.[55] In our case, the impregnated but non-laser-processed sample (0 pulses) shows a strongly inhibited activity compared to the pristine Co_3O_4 most likely due to the formation of insulating iron (oxy)hydroxide layer/clusters[40,41] after adsorption of the iron precursor on impregnation, which resembles a very high iron concentration in the catalytically relevant first outer surface layer. This insulating layer hampers the charge transfer and is detrimental to overall OER activity. With the increasing number of laser pulses, similar to the results in 2-propanol oxidation, the OER activity of the samples also increases due to the incorporation of iron into the spinel surface and diminishing the detrimental iron (oxy)-hydroxide clusters.

Considering the catalytic stability, the sample treated with 4 pulses is less prone to deactivation when comparing the initial activity after the 1st cycle and the 50th cycle (compare Figure S14c,d at 4 laser pulses). Interestingly, even the pure Co_3O_4 catalyst shows slight deactivation after 50 cycles, which is likely related to the expected phase transformation of Co_3O_4 in the surface region to $CoO_x(OH)_y$, during the electrochemical conditioning.[55,56] The incorporation of Fe by laser doping might increase the stability of the Co_3O_4 phase, which was also found in previous investigations of Fe-doped Co_3O_4.[16] However, it is also thinkable that the laser excitation in water results in a preconditioned and more stable catalyst due to the generation of surface hydroxides.[35,37] In turn, the sample that was impregnated with $FeCl_3$ but without further application of laser pulses (compare Figure S14c,d at 0 laser pulses) shows a particular deactivation after 50 voltammetry cycles. The deactivation might be correlated to the existence of iron (oxy)hydroxide clusters on the surface of the catalyst, which are prone to be deactivated in a harsh alkaline environment due to leaching or oxidation into a soluble FeO_4^{2-} at a high anodic potential as suggested by the Pourbaix diagram.[17,55,57−59] This increasing resistance to the deactivation on 4 laser pulses further indicates that the laser processing successfully induces the incorporation of iron into the spinel surface and creates a stable iron-doped spinel phase.

■ CONCLUSIONS

In this study, we investigated the pulse-by-pulse laser doping of colloidal Co_3O_4 nanoparticles with impregnated aqueous iron salt precursors under repeated single laser pulse excitation using a flat liquid jet setup and uniform irradiation conditions. Before the first laser pulse was applied, HR-TEM showed that the iron cations from the $FeCl_3$ precursor solution adsorbed onto the Co_3O_4 surface and form small clusters (1−3 nm) of iron oxyhydroxide after sample preparation (drying) and subsequent washing. These surface clusters were observed to disappear upon laser treatment of the impregnated colloidal Co_3O_4 nanoparticles with the first single laser pulse while forming a disordered surface layer. Similar disordered layers were also reported after laser-based defect-writing of colloidal $CoFe_2O_4$ nanoparticles.[37] XRF as a bulk-sensitive quantification method shows a constant iron concentration of ~9 wt % in the laser-doped catalysts over several individual laser pulses. Accordingly, XPS resembling a surface-sensitive method shows the same trends as XRF but with more than 2× the iron content since the iron is concentrated on the surface. XRD indicates a steady increase of the lattice parameter with laser processing and dopant concentration, indicating the incorporation of iron throughout the sequentially pulsed laser doping. A comparison to the lattice parameter of the laser-doped samples with $CoFe_2O_4$ and Fe_3O_4 is in agreement with an average of 1−2 atom % embedded Fe atoms. However, close to the surface, significantly higher Fe concentrations are expected, as indicated by XPS. Magnetometry measurements of impregnated but non-laser-processed Co_3O_4 showed the characteristic antiferromagnetic behavior of spinel Co_3O_4 with barely any hysteresis and low coercivity. After individual laser pulses were employed pulse-by-pulse to the impregnated colloidal Co_3O_4, the hysteresis and coercivity gradually increase with the number of laser pulses exhibiting the largest increase after the first laser pulse. The same trend is observed in Mössbauer spectroscopy, showing an increase in the mean spin canting angle with a rising number of subsequently employed laser pulses. Both observations show that an increasing interaction of the Fe cations with the antiferromagnetic Co_3O_4 support occurred after individual laser pulses were employed, supporting (in line with XRD) that a laser-induced cation doping occurred. Since nanosecond laser pulses were employed throughout the doping process, only very short heating and hence diffusion duration of several tens of nanoseconds had to be expected. To evaluate if a laser-induced diffusion of the iron cation into a laser-heated Co_3O_4 represents a realistic scenario for pulse-by-pulse laser doping of colloidal nanoparticles, the achievable diffusion depth after laser excitation was estimated by solving Fick's second law at previously calculated typical laser-induced particle temperature of ~1000 K,[35] related diffusion constants,[49] and estimated duration at this temperature hot colloidal nanoparticle of ~20 ns per laser pulse.[53] The results suggest that for a doping depth of 1 nm, a mole fraction of 1% Fe is reached after the first laser pulse. After the fourth laser pulse, iron is expected to have diffused roughly 2 nm into the Co_3O_4 nanoparticle surface. Furthermore, a logarithmic increase of the doping depth with an increasing number of applied laser pulses was found from the calculations, which is in good agreement with the trends observed for the coercivity and spin canting angle determined from magnetometry and Mössbauer spectroscopy, respectively, supporting the interpretation of a successful laser cation doping of colloidal nanoparticles. To evaluate the applicability of a gradually laser-modified series of Co iron-doped Co_3O_4 catalysts, the material series was finally tested regarding their catalytic activity in gas-phase isopropanol oxidation and liquid-phase OER. The observed catalytic activity trends of the laser-doped catalysts were in good agreement with previously published composition series gained from different impregnation techniques used to synthesize a nanoparticulate Fe:Co catalyst composition series. These results demonstrate that laser-induced cation doping provides gradually surface-doped catalysts with maintained surface area and particle size, rendering laser-induced doping **comparable and complementary** to conventional synthesis methods.[5−7] Reusability tests further showed **good catalytic stability** of the catalysts after the first, as well as subsequent laser pulses, while non-laser-processed catalysts deactivated in the OER most likely due to leaching and detrimental oxidation processes. For both reactions, the catalytic activity of the pulse-by-pulse laser-doped iron-impregnated Co_3O_4 catalysts was found to gradually increase with the rising number of employed individual laser pulses. When referencing the catalytic activity of the sample series with the expected thermally induced doping depth, a linear improvement of the catalytic activity was observed for both reaction types, highlighting an imminent strength of laser doping in providing a **gradual catalyst doping series** to study and identify composition-related active sites and reaction mechanisms in future catalytic studies. Overall, this paper demonstrates the feasibility of pulse-by-pulse laser surface cation doping of colloidal nanoparticles to provide comparable, active, and stable catalyst series to investigate composition-dependent catalytic activity profiles and identify active sites and reaction mechanisms in future catalytic studies.

■ ASSOCIATED CONTENT

Supporting Information

The Supporting Information is available free of charge at https://pubs.acs.org/doi/10.1021/acs.jpcc.2c01753.

Measured laser beam profile used during laser doping; HR-TEM/EDX profiles of Co_3O_4 doped with 0.5 mmol $^{57}FeCl_3$; iron loading before and after single laser pulse doping of Co_3O_4 in different $FeCl_3$ concentrations; XPS survey, Co2p, and Fe2p spectra of Co_3O_4 before and after laser doping with 1−4 pulses and in 2 mmol/L as well as 0.5 mmol/L $FeCl_3$; XRD pattern of Co_3O_4 before and after laser doping with 1−4 laser pulses within 2 mmol $FeCl_3$, 0.5 mmol $FeCl_3$ solution, and related Rietveld refinement parameters, respectively; magnetic hysteresis measurements at 4.3 K; temperature-dependent magnetization measurement; individual Mössbauer spectra; and stacked Mössbauer spectra as well as thereof derived line ratio A_{23} of Co_3O_4 laser-doped within a 0.5 mmol/L $^{57}FeCl_3$ solution, respectively; scheme of the used in situ DRIFTS setup for catalytic 2-propanol oxidation; measured in situ DRIFTS spectra during isopropanol oxidation at different temperatures as well as description of the performed data analysis; temperature-dependent activity profiles derived from the in situ DRIFTS spectra; linear sweep voltammograms of Fe-doped Co_3O_4 catalysts (PDF)

■ AUTHOR INFORMATION

Corresponding Authors

Stephan Barcikowski − *Center for Nanointegration Duisburg-Essen (CENIDE), University of Duisburg-Essen, 47057 Duisburg, Germany; Technical Chemistry I, University of Duisburg-Essen, 45141 Essen, Germany;* orcid.org/0000-0002-9739-7272; Email: Stephan.Barcikowski@uni-due.de

Sven Reichenberger − *Center for Nanointegration Duisburg-Essen (CENIDE), University of Duisburg-Essen, 47057 Duisburg, Germany; Technical Chemistry I, University of Duisburg-Essen, 45141 Essen, Germany;* orcid.org/0000-0002-7166-9428; Email: Sven.Reichenberger@uni-due.de

Authors

Swen Zerebecki – *Center for Nanointegration Duisburg-Essen (CENIDE), University of Duisburg-Essen, 47057 Duisburg, Germany; Technical Chemistry I, University of Duisburg-Essen, 45141 Essen, Germany*

Kai Schott – *Center for Nanointegration Duisburg-Essen (CENIDE), University of Duisburg-Essen, 47057 Duisburg, Germany; Technical Chemistry I, University of Duisburg-Essen, 45141 Essen, Germany*

Soma Salamon – *Center for Nanointegration Duisburg-Essen (CENIDE), University of Duisburg-Essen, 47057 Duisburg, Germany; Faculty of Physics, University of Duisburg-Essen, 47057 Duisburg, Germany*

Joachim Landers – *Center for Nanointegration Duisburg-Essen (CENIDE), University of Duisburg-Essen, 47057 Duisburg, Germany; Faculty of Physics, University of Duisburg-Essen, 47057 Duisburg, Germany*

Heiko Wende – *Center for Nanointegration Duisburg-Essen (CENIDE), University of Duisburg-Essen, 47057 Duisburg, Germany; Faculty of Physics, University of Duisburg-Essen, 47057 Duisburg, Germany;* orcid.org/0000-0001-8395-3541

Eko Budiyanto – *Max-Planck-Institut für Kohlenforschung, 45470 Mülheim an der Ruhr, Germany*

Harun Tüysüz – *Max-Planck-Institut für Kohlenforschung, 45470 Mülheim an der Ruhr, Germany;* orcid.org/0000-0001-8552-7028

Complete contact information is available at:
https://pubs.acs.org/10.1021/acs.jpcc.2c01753

Notes

The authors declare no competing financial interest.

■ ACKNOWLEDGMENTS

We gratefully acknowledge the DFG Deutsche Forschungsgemeinschaft for its financial support under Project 388390466 - TRR 247 (sub-projects B2, C1, C5, and S). Dr. Marcus Heidelmann (ICAN) and Jurji Jacobi are acknowledged for assistance with HR-TEM measurements. HT thanks Max Planck Society for the basic funding.

■ REFERENCES

(1) Deo, G., Cherian, M., Rao, T. V. M.*Metal oxides:Chemistry and applications*; Taylor & Francis, 2006.

(2) Parravano, G. The Catalytic Oxidation of Carbon Monoxide on Nickel Oxide. II. Nickel Oxide Containing Foreign Ions. *J. Am. Chem. Soc.* **1953**, *75*, 1452–1454.

(3) McFarland, E. W.; Metiu, H. Catalysis by doped oxides. *Chem. Rev.* **2013**, *113*, 4391–4427.

(4) Anke, S.; Falk, T.; Bendt, G.; Sinev, I.; Hävecker, M.; Antoni, H.; Zegkinoglou, I.; Jeon, H.; Knop-Gericke, A.; Schlögl, R.; Roldan Cuenya, B.; Schulz, S.; Muhler, M. On the reversible deactivation of cobalt ferrite spinel nanoparticles applied in selective 2-propanol oxidation. *J. Catal.* **2020**, *382*, 57–68.

(5) Budiyanto, E.; Yu, M.; Chen, M.; DeBeer, S.; Rüdiger, O.; Tüysüz, H. Tailoring Morphology and Electronic Structure of Cobalt Iron Oxide Nanowires for Electrochemical Oxygen Evolution Reaction. *ACS Appl. Energy Mater.* **2020**, *3*, 8583–8594.

(6) Waffel, D.; Budiyanto, E.; Porske, T.; Büker, J.; Falk, T.; Fu, Q.; Schmidt, S.; Tüysüz, H.; Muhler, M.; Peng, B. Investigation of Synergistic Effects between Co and Fe in Co3-xFexO4 Spinel Catalysts for the Liquid-Phase Oxidation of Aromatic Alcohols and Styrene. *Mol. Catal.* **2020**, *498*, 111251.

(7) Falk, T.; Budiyanto, E.; Dreyer, M.; Pflieger, C.; Waffel, D.; Büker, J.; Weidenthaler, C.; Ortega, K. F.; Behrens, M.; Tüysüz, H.; Muhler, M.; Peng, B. Identification of Active Sites in the Catalytic Oxidation of 2-Propanol over Co 1+x Fe 2−x O 4 Spinel Oxides at Solid/Liquid and Solid/Gas Interfaces. *ChemCatChem* **2021**, *13*, 2942–2951.

(8) Waag, F.; Gökce, B.; Kalapu, C.; Bendt, G.; Salamon, S.; Landers, J.; Hagemann, U.; Heidelmann, M.; Schulz, S.; Wende, H.; Hartmann, N.; Behrens, M.; Barcikowski, S. Adjusting the catalytic properties of cobalt ferrite nanoparticles by pulsed laser fragmentation in water with defined energy dose. *Sci. Rep.* **2017**, *7*, 13161.

(9) Yu, M.; Waag, F.; Chan, C. K.; Weidenthaler, C.; Barcikowski, S.; Tüysüz, H. Laser fragmentation induced defect-rich cobalt oxide nanoparticles for electrochemical oxygen evolution reaction. *ChemSusChem* **2020**, 520.

(10) Saddeler, S.; Hagemann, U.; Schulz, S. Effect of the Size and Shape on the Electrocatalytic Activity of Co3O4 Nanoparticles in the Oxygen Evolution Reaction. *Inorg. Chem.* **2020**, *59*, 10013–10024.

(11) Chakrapani, K.; Bendt, G.; Hajiyani, H.; Schwarzrock, I.; Lunkenbein, T.; Salamon, S.; Landers, J.; Wende, H.; Schlögl, R.; Pentcheva, R.; Behrens, M.; Schulz, S. Role of Composition and Size of Cobalt Ferrite Nanocrystals in the Oxygen Evolution Reaction. *ChemCatChem* **2017**, *9*, 2988–2995.

(12) Quast, T.; Varhade, S.; Saddeler, S.; Chen, Y.-T.; Andronescu, C.; Schulz, S.; Schuhmann, W. Single Particle Nanoelectrochemistry Reveals the Catalytic Oxygen Evolution Reaction Activity of Co3O4 Nanocubes. *Angew. Chem. Int. Ed.* **2021**, DOI: 10.1002/anie.202109201.

(13) El Arrassi, A.; Liu, Z.; Evers, M. V.; Blanc, N.; Bendt, G.; Saddeler, S.; Tetzlaff, D.; Pohl, D.; Damm, C.; Schulz, S.; et al. Intrinsic Activity of Oxygen Evolution Catalysts Probed at Single CoFe2O4 Nanoparticles. *J. Am. Chem. Soc.* **2019**, *141*, 9197–9201.

(14) Anke, S.; Bendt, G.; Sinev, I.; Hajiyani, H.; Antoni, H.; Zegkinoglou, I.; Jeon, H.; Pentcheva, R.; Roldan Cuenya, B.; Schulz, S.; Muhler, M. Selective 2-Propanol Oxidation over Unsupported Co 3 O 4 Spinel Nanoparticles: Mechanistic Insights into Aerobic Oxidation of Alcohols. *ACS Catal.* **2019**, *9*, 5974–5985.

(15) Hung, S.-F.; Hsu, Y.-Y.; Chang, C.-J.; Hsu, C.-S.; Suen, N.-T.; Chan, T.-S.; Chen, H. M. Unraveling Geometrical Site Confinement in Highly Efficient Iron-Doped Electrocatalysts toward Oxygen Evolution Reaction. *Adv. Energy Mater.* **2018**, *8*, No. 1701686.

(16) Xiao, C.; Lu, X.; Zhao, C. Unusual synergistic effects upon incorporation of Fe and/or Ni into mesoporous Co3O4 for enhanced oxygen evolution. *Chem. Commun.* **2014**, *50*, 10122–10125.

(17) Xiang, W.; Yang, N.; Li, X.; Linnemann, J.; Hagemann, U.; Ruediger, O.; Heidelmann, M.; Falk, T.; Aramini, M.; DeBeer, S.; Muhler, M.; Tschulik, K.; Li, T. 3D atomic-scale imaging of mixed Co-Fe spinel oxide nanoparticles during oxygen evolution reaction. *Nat. Commun.* **2022**, *13*, 179.

(18) Gao, X.; Liu, J.; Sun, Y.; Wang, X.; Geng, Z.; Shi, F.; Wang, X.; Zhang, W.; Feng, S.; Wang, Y.; Huang, K. Optimized Co 2+(Td) −O−Fe 3+(Oh) electronic states in a spinel electrocatalyst for highly efficient oxygen evolution reaction performance. *Inorg. Chem. Front.* **2019**, *6*, 3295–3301.

(19) Krstulović, N.; Salamon, K.; Budimlija, O.; Kovač, J.; Dasović, J.; Umek, P.; Capan, I. Parameters optimization for synthesis of Al-doped ZnO nanoparticles by laser ablation in water. *Appl. Surf. Sci.* **2018**, *440*, 916–925.

(20) Ludwig, A. Discovery of new materials using combinatorial synthesis and high-throughput characterization of thin-film materials libraries combined with computational methods. *npj Comput. Mater.* **2019**, *5*, 70.

(21) Zolper, J. C.; Wilson, R. G.; Pearton, S. J.; Stall, R. A. Ca and O ion implantation doping of GaN. *Appl. Phys. Lett.* **1996**, *68*, 1945–1947.

(22) Hallam, B.; Chan, C.; Sugianto, A.; Wenham, S. Deep junction laser doping for contacting buried layers in silicon solar cells. *Sol. Energy Mater. Sol. Cells* **2013**, *113*, 124–134.

(23) Amendola, V.; Amans, D.; Ishikawa, Y.; Koshizaki, N.; Scirè, S.; Compagnini, G.; Reichenberger, S.; Barcikowski, S. Room-Temperature Laser Synthesis in Liquid of Oxide, Metal-Oxide Core-Shells, and Doped Oxide Nanoparticles. *Chem. −A Eur. J.* **2020**, DOI: 10.1002/chem.202000686.

(24) Dalpian, G. M.; Chelikowsky, J. R. Self-purification in semiconductor nanocrystals. *Phys. Rev. Lett.* **2006**, *96*, No. 226802.

(25) Carey, P. G.; Sigmon, T. W. In-situ doping of silicon using the gas immersion laser doping (GILD) process. *Appl. Surf. Sci.* **1989**, *43*, 325−332.

(26) Bet, S.; Quick, N.; Kar, A. Effect of laser field and thermal stress on diffusion in laser doping of SiC. *Acta Mater.* **2007**, *55*, 6816−6824.

(27) Lin, Z.; Du, C.; Yan, B.; Wang, C.; Yang, G. Two-dimensional amorphous NiO as a plasmonic photocatalyst for solar H2 evolution. *Nat. Commun.* **2018**, *9*, 4036.

(28) Chemin, A.; Lam, J.; Laurens, G.; Trichard, F.; Motto-Ros, V.; Ledoux, G.; Jarý, V.; Laguta, V.; Nikl, M.; Dujardin, C.; Amans, D. Doping nanoparticles using pulsed laser ablation in a liquid containing the doping agent. *Nanoscale Adv.* **2019**, *1*, 3963−3972.

(29) Kanakkillam, S. S.; Shaji, S.; Krishnan, B.; Vazquez-Rodriguez, S.; Martinez, J. A.; Palma, M. M.; Avellaneda, D. A. Nanoflakes of zinc oxide:cobalt oxide composites by pulsed laser fragmentation for visible light photocatalysis. *Appl. Surf. Sci.* **2020**, *501*, No. 144223.

(30) Nakamura, M.; Oyane, A.; Sakamaki, I.; Ishikawa, Y.; Shimizu, Y.; Kawaguchi, K. Laser-assisted one-pot fabrication of calcium phosphate-based submicrospheres with internally crystallized magnetite nanoparticles through chemical precipitation. *Phys. Chem. Chem. Phys.* **2015**, *17*, 8836−8842.

(31) Nakamura, M.; Oyane, A.; Shimizu, Y.; Miyata, S.; Saeki, A.; Miyaji, H. Physicochemical fabrication of antibacterial calcium phosphate submicrospheres with dispersed silver nanoparticles via coprecipitation and photoreduction under laser irradiation. *Acta Biomater.* **2016**, *46*, 299−307.

(32) Liang, S.-X.; Salamon, S.; Zerebecki, S.; Zhang, L.-C.; Jia, Z.; Wende, H.; Reichenberger, S.; Barcikowski, S. A laser-based synthesis route for magnetic metallic glass nanoparticles. *Scr. Mater.* **2021**, *203*, No. 114094.

(33) Liang, S.-X.; Zhang, L.-C.; Reichenberger, S.; Barcikowski, S. Design and perspective of amorphous metal nanoparticles from laser synthesis and processing. *Phys. Chem. Chem. Phys.* **2021**, *23*, 11121−11154.

(34) Peng, Y.; Cao, J.; Sha, Y.; Yang, W.; Li, L.; Liu, Z. Laser solid-phase synthesis of single-atom catalysts. *Light Sci. Appl.* **2021**, *10*, 168.

(35) Budiyanto, E.; Zerebecki, S.; Weidenthaler, C.; Kox, T.; Kenmoe, S.; Spohr, E.; DeBeer, S.; Rüdiger, O.; Reichenberger, S.; Barcikowski, S.; Tüysüz, H. Impact of Single-Pulse, Low-Intensity Laser Post-Processing on Structure and Activity of Mesostructured Cobalt Oxide for the Oxygen Evolution Reaction. *ACS Appl. Mater. Interfaces* **2021**, DOI: 10.1021/acsami.1c08034.

(36) Zerebecki, S.; Reichenberger, S.; Barcikowski, S. Continuous-Flow Flat Jet Setup for Uniform Pulsed Laser Postprocessing of Colloids. *J. Phys. Chem. A* **2020**, *124*, 11125−11132.

(37) Zerebecki, S.; Salamon, S.; Landers, J.; Yang, Y.; Tong, Y.; Budiyanto, E.; Waffel, D.; Dreyer, M.; Saddeler, S.; Kox, T.; et al. Engineering of Cation Occupancy of CoFe 2 O 4 Oxidation Catalysts by Nanosecond, Single-Pulse Laser Excitation in Water. *ChemCatChem* **2022**, *14*, No. e202101785.

(38) Oriekhova, O.; Stoll, S. Investigation of FeCl3 induced coagulation processes using electrophoretic measurement, nanoparticle tracking analysis and dynamic light scattering: Importance of pH and colloid surface charge. *Colloids Surf., A* **2014**, *461*, 212−219.

(39) https://www.uni-due.de/~hm236ap/hoersten/home.html.

(40) Gilbert, B.; Lu, G.; Kim, C. S. Stable cluster formation in aqueous suspensions of iron oxyhydroxide nanoparticles. *J. Colloid Interface Sci.* **2007**, *313*, 152−159.

(41) Fu, D.; Keech, P. G.; Sun, X.; Wren, J. C. Iron oxyhydroxide nanoparticles formed by forced hydrolysis: dependence of phase composition on solution concentration. *Phys. Chem. Chem. Phys.* **2011**, *13*, 18523−18529.

(42) Vaz, C. A. F.; Prabhakaran, D.; Altman, E. I.; Henrich, V. E. Experimental study of the interfacial cobalt oxide in Co3O4/α−Al2O3(0001) epitaxial films. *Phys. Rev. B* **2009**, *80*, No. 155457.

(43) Kaufmann, M.; Mantler, M.; Weber, F. Analysis of Multi-Layer Thin Films by XRF. *Adv. X-Ray Anal.* **1993**, *37*, 205−212.

(44) Landers, J.; Salamon, S.; Webers, S.; Wende, H. Microscopic understanding of particle-matrix interaction in magnetic hybrid materials by element-specific spectroscopy. *Phys. Sci. Rev.* **2020**, No. 20190116.

(45) Ziefuss, A. R.; Reich, S.; Reichenberger, S.; Levantino, M.; Plech, A. In situ structural kinetics of picosecond laser-induced heating and fragmentation of colloidal gold spheres. *Phys. Chem. Chem. Phys.* **2020**, *22*, 4993−5001.

(46) Jost, W. *Diffusion in Solids, Liquid, Gases*; Academic Press, 1960; p. 73.

(47) Cussler, E. L. *Diffusion:Mass transfer in fluid systems*, 2nd ed., reprint; Cambridge series in chemical engineering; Cambridge Univ. Press, 2000.

(48) Jacobs, M. H. *Diffusion Processes*; Springer, 1967.

(49) Grzesik, Z.; Kaczmarska, A.; Mrowec, S. Nonstoichiometry and Chemical Diffusion in Co_3O_4 Cobalt Oxide. *Solid State Phenom.* **2015**, *227*, 421−424.

(50) Barreca, D.; Massignan, C.; Daolio, S.; Fabrizio, M.; Piccirillo, C.; Armelao, L.; Tondello, E. Composition and Microstructure of Cobalt Oxide Thin Films Obtained from a Novel Cobalt(II) Precursor by Chemical Vapor Deposition. *Chem. Mater.* **2001**, *13*, 588−593.

(51) Ravi Dhas, C.; Venkatesh, R.; Jothivenkatachalam, K.; Nithya, A.; Suji Benjamin, B.; Moses Ezhil Raj, A.; Jeyadheepan, K.; Sanjeeviraja, C. Visible light driven photocatalytic degradation of Rhodamine B and Direct Red using cobalt oxide nanoparticles. *Ceram. Int.* **2015**, *41*, 9301−9313.

(52) Waegele, M. M.; Doan, H. Q.; Cuk, T. Long-Lived Photoexcited Carrier Dynamics of d − d Excitations in Spinel Ordered Co 3 O 4. *J. Phys. Chem. C* **2014**, *118*, 3426−3432.

(53) Furlani, E. P.; Karampelas, I. H.; Xie, Q. Analysis of pulsed laser plasmon-assisted photothermal heating and bubble generation at the nanoscale. *Lab Chip* **2012**, *12*, 3707−3719.

(54) Hsu, S.-H.; Hung, S.-F.; Wang, H.-Y.; Xiao, F.-X.; Zhang, L.; Yang, H.; Chen, H. M.; Lee, J.-M.; Liu, B. Tuning the Electronic Spin State of Catalysts by Strain Control for Highly Efficient Water Electrolysis. *Small Methods* **2018**, *2*, No. 1800001.

(55) Burke, M. S.; Kast, M. G.; Trotochaud, L.; Smith, A. M.; Boettcher, S. W. Cobalt-iron (oxy)hydroxide oxygen evolution electrocatalysts: the role of structure and composition on activity, stability, and mechanism. *J. Am. Chem. Soc.* **2015**, *137*, 3638−3648.

(56) Bergmann, A.; Martinez-Moreno, E.; Teschner, D.; Chernev, P.; Gliech, M.; de Araújo, J. F.; Reier, T.; Dau, H.; Strasser, P. Reversible amorphization and the catalytically active state of crystalline Co3O4 during oxygen evolution. *Nat. Commun.* **2015**, *6*, 8625.

(57) Luo, W.; Jiang, C.; Li, Y.; Shevlin, S. A.; Han, X.; Qiu, K.; Cheng, Y.; Guo, Z.; Huang, W.; Tang, J. Highly crystallized α-FeOOH for a stable and efficient oxygen evolution reaction. *J. Mater. Chem. A* **2017**, *5*, 2021−2028.

(58) Zou, S.; Burke, M. S.; Kast, M. G.; Fan, J.; Danilovic, N.; Boettcher, S. W. Fe (Oxy)hydroxide Oxygen Evolution Reaction Electrocatalysis: Intrinsic Activity and the Roles of Electrical Conductivity, Substrate, and Dissolution. *Chem. Mater.* **2015**, *27*, 8011−8020.

(59) Beverskog, B.; Puigdomenech, I. Revised pourbaix diagrams for iron at 25−300 °C. *Corros. Sci.* **1996**, *38*, 2121−2135.